Thermodynamic Analysis and Crystallographic Properties of MFe_2O_4, MCr_2O_4 and MAl_2O_4 (M = Fe, Ni, Zn) Formed on Structural Materials in Pressurized Water Reactor Primary Circuit under Zinc and Zinc-aluminum Water Chemistry

Yang Jiao [1,2], Shenghan Zhang [1,2,*] and Yu Tan [1,2]

1   Hebei Key Lab of Power Plant Flue Gas Multi-Pollutants Control, Department of Environmental Science and Engineering, North China Electric Power University, Baoding 071003, China; 1182102069@ncepu.edu.cn (Y.J.); lucifertan@163.com (Y.T.)
2   Environmental System Optimization, College of Environmental Science and Engineering, North China Electric Power University, Beijing 102206, China
*   Correspondence: zhangsh@ncepu.edu.cn; Tel.: +86-13930237597

Abstract: Zinc injection technology (zinc water chemistry, ZWC) was widely applied in pressurized water reactor (PWR) primary circuits to reduce radiation buildup and improve corrosion resistance of structural materials. The simultaneous injection of zinc-aluminium (ZAWC) is a novel implement created to replace part of Zn^{2+} by Al^{3+}. It was reported ZAWC can improve further corrosion resistance of carbon steels and stainless steels. However, ZAWC sometimes showed even negative effects on Nickel-alloys. In this study, mechanism of formation of oxide film on metals was investigated. The reactions of Fe^{2+} Ni^{2+} in oxide films replaced by Zn^{2+}, or Fe^{3+} replaced by Al^{3+} in ZAWC were analysed. The thermodynamic data and solubility of mixed oxides ($ZnFe_2O_4$, $ZnCr_2O_4$, and $ZnAl_2O_4$), the products of replace reactions, were calculated. According to the Gibbs free energy difference between products and reactants, $\Delta G^{\theta}(T)$ values of the formation reaction of $ZnFe_2O_4$, $ZnCr_2O_4$, and $ZnAl_2O_4$ are extremely negative. Solubility of $ZnAl_2O_4$ is the lowest among mixed oxide products, which implies the oxide film composites of $ZnAl_2O_4$ may show a lower corrosion rate. In addition, the preferential formation of $NiAl_2O_4$ on Ni-based-alloy, under ZAWC, was discussed based on crystallographic properties of spinel, which was considered as the cause of negative effects of ZAWC on corrosion resistance of Nickel-alloys. This research provides an analytical basis for the study of thermodynamic stability of oxide films under different chemical chemistry and a theoretical basis for improving corrosion resistance of different metals and optimizing the chemical conditions of PWR primary circuit.

Keywords: thermodynamic property; solubility; zinc injection; zinc-aluminium simultaneous injection; oxide film; PWR primary circuit

1. Introduction

Light water reactors (LWR) and pressurized heavy water reactors (PHWR) are the main reactor types of nuclear power plants. LWR are divided into pressurized water reactors and boiling water reactors (BWR). The main materials in PWR primary system (Figure 1) are composed of 25% zirconium alloys as fuel cladding, 65% Ni-based alloys as steam generator (SG) tubes, 5% stainless steels (SS) as SG, and some carbon steels (CS). At the same time, stainless steels are also the main materials of piping in PWR primary circuit [1,2].

The component materials in PWR primary circuit are listed in Table 1. Based on PWR primary coolant water chemistry conditions, it has been reported that iron oxides are the main component in oxide films formed on carbon steels. It was also well known that

oxide films, formed on stainless and nickel-based alloys in high temperature water, had a double-layer structure: a (Ni, Fe)-rich outer layer and a Cr-rich inner layer [3–6].

Table 1. Component materials in PWR primary system (%).

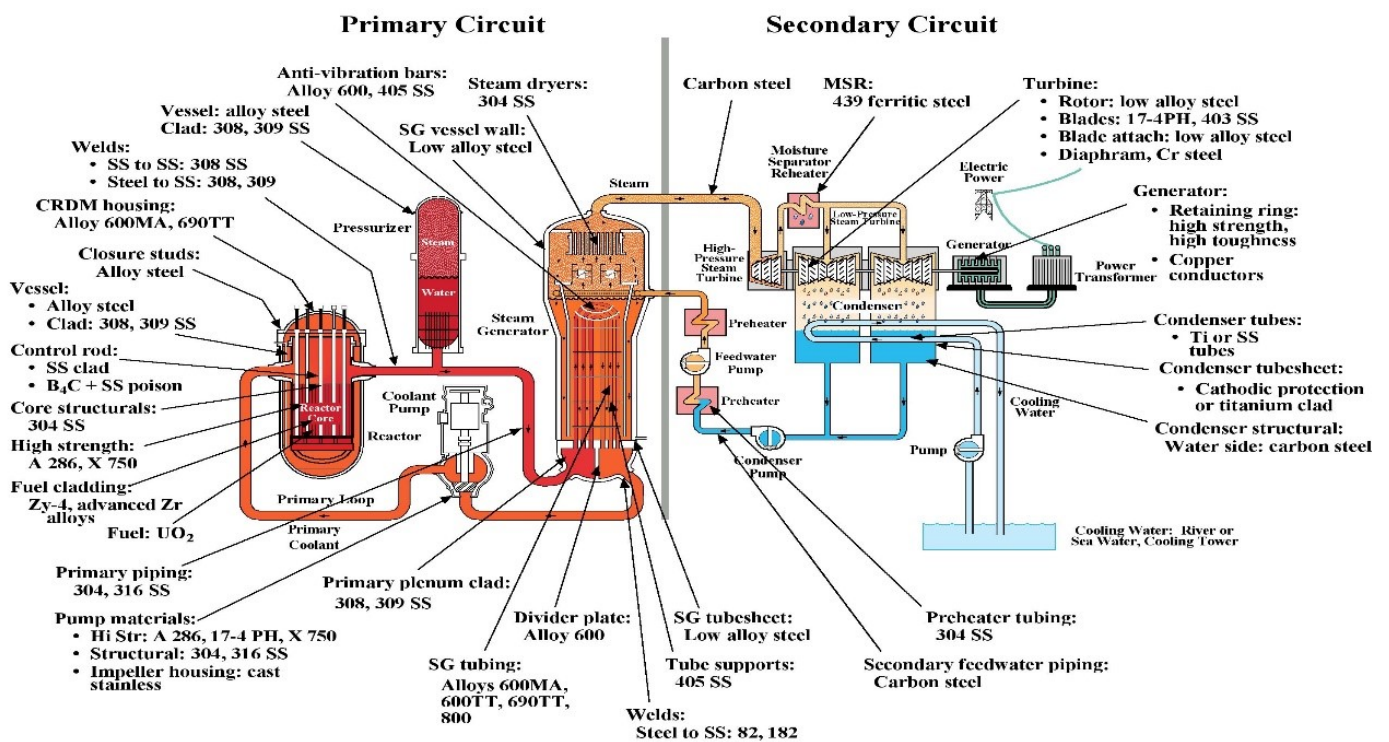|	Composition (%)				
	C	**Cr**	**Ni**	**Fe**	**Mn**
A106B CS	≤0.3	≤0.4	≤0.4	Bal.	0.29–1.06
A508-3 CS	≤0.22	≤0.25	0.5–0.80	Bal.	1.15–1.6
304L SS	≤0.03	18–20	8–12	Bal.	≤2.0
316L SS	≤0.03	16–18	10–14	Bal.	≤2.0
Incoloy 800	≤0.1	19–23	30–35	37–47	≤1.5
Inconel 600	≤0.15	14–17	72	6–10	≤1.0
Inconel 690	0.023	30.39	60	8.88	0.23

Figure 1. Distribution of structural materials used in PWRs [7].

The corrosion and radiation buildup reduction effects of zinc injection into PWR primary coolant has been experimentally and practically confirmed in past years [8–11]. As the improvement plan of zinc injection technology, the inhibitory effects of simultaneous injection of zinc and aluminium, on the general corrosion of different metal materials, has also been proved in the previous studies in recent years. However, the influence on different materials were different. Zhang et al. [12] claimed that the corrosion resistance of oxide films, formed on 316L SS in this new technology, was significantly improved compared than zinc injection. In the research of Sun [13], it has been pointed out that the effects of ZAWC on the corrosion behaviour of carbon steel, stainless steel, and Ni-based alloy were different. Compared with conventional water chemistry, the corrosion current density of oxide film formed on A508-3 CS reduced by 30% under ZWC, but almost 75% for 304L SS. After zinc-aluminium was simultaneously injected into boron-lithium solution, the corrosion resistance of CS and SS was significantly enhanced, and the corrosion current density could be reduced by an order of magnitude, but the improvement effect was weak for Ni-based alloys. The specific effects of these two implements on the corrosion current density were shown in Figure 2, in which "PWR" represents the common PWR coolant

water chemistry, and, assuming that the corrosion current density in this environment was 100%, the percentage shown in the vertical axis was relative to the value of PWR.
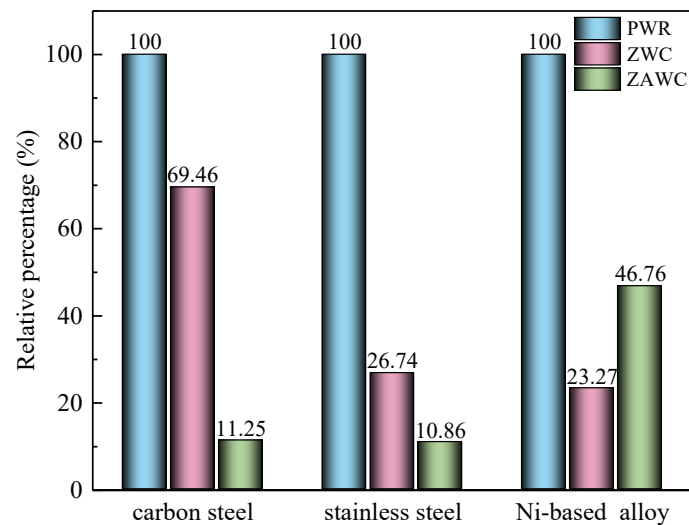

Figure 2. Effects of ZWC and ZAWC on the corrosion of different materials [13].

The previous results were obtained, mainly, through experiments, especially for the condition of ZAWC. However, no detailed mechanism analysis was carried out for the explanation of differences between different types of metal materials. The consideration of oxide composition under high temperature aqueous conditions is fundamental to the corrosion behaviour and stability of alloys. In order to evaluate the effectiveness of zinc and zinc-aluminium injection on the corrosion behaviour of carbon steels, stainless steels, and Ni-based alloys, thermodynamic data and solubility calculation at high temperatures are carried out to compare the thermal stability of oxide films formed on metal surface. Based on the Laws of Thermodynamics, the lower value of Gibbs free energy at high temperatures means the high thermodynamic stability of substance. When the Gibbs free energy difference between products and reactants of reactions is less than zero, it indicates that the reaction between oxide film and solution can proceed spontaneously, and the more negative the value, the higher degree of spontaneity. Moreover, the parameters and crystallographic features of spinel are suggested to illustrate the preference of different cation ions, which can judge the structural stability of spinel oxides formed on the surface of metals.

2. Thermodynamic

The composition of oxide films formed on different materials in simulated PWR primary coolant have been confirmed in previous researches. The effect of the injection of different ions into the coolant of PWR primary circuit on the oxide film on the metal surface and the mechanism diagram are shown in Figure 3. In PWR primary circuit, passive films with large polyhedral oxides form on carbon steels. Generally, the oxides are mainly composites of iron oxides and minor other metal oxides. After Zn^{2+} added into primary circuit, Zn^{2+} was incorporated into the oxide films, and finally, small-size polyhedral oxides (mixed oxides of iron and zinc) formed on the surface. However, due to the low concentration of Zn^{2+}, a number of large polyhedral also exist. On the condition of Zn^{2+} and Al^{3+} simultaneous injection, Al^{3+} may enter the oxide film through substitution reactions. Generally, oxide films, formed on stainless steels and Ni-based alloys in high temperature water, have a duplex structure with a Cr-rich inner layer and Cr-depleted outer layer. Under ZWC and ZAWC conditions, Zn^{2+} and Al^{3+} can also participate in the reactions to form smaller and denser protective oxides.
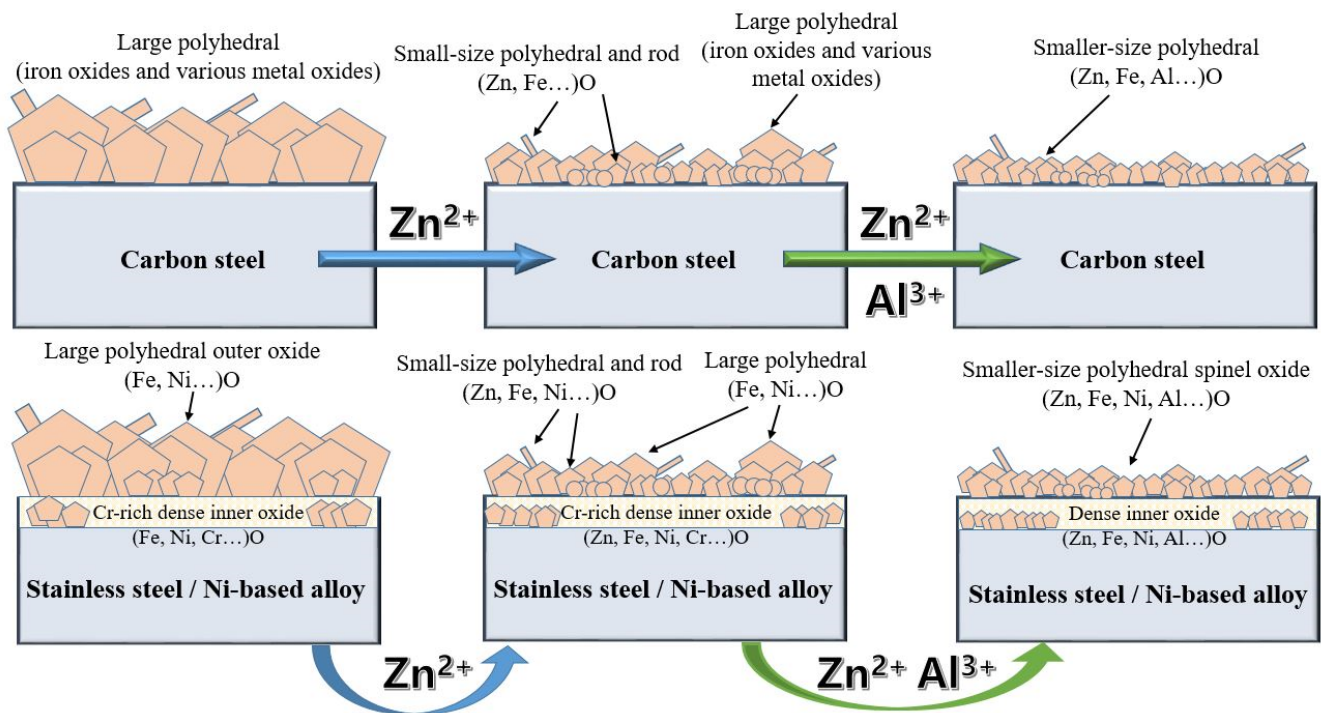
Figure 3. The mechanism diagram of the oxide formed on metals in PWR circuit with zinc and zinc-aluminium simultaneous injection.
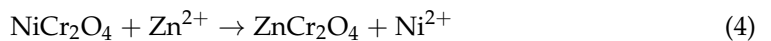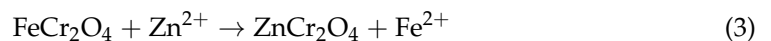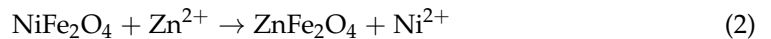
The specific analysis and the thermodynamic calculation of the formation reaction of various substances are studied in this chapter.

2.1. Zinc Injection

It has been generally acknowledged that iron oxides (Fe_3O_4, Fe_2O_3, FeO . . .) were the main oxides on carbon steels that protect the surface from corrosion. When dozens of ppb Zn^{2+} are added to primary coolant, $ZnFe_2O_4$ may be generated by Reaction (1):

$$Fe_3O_4 + Zn^{2+} \rightarrow ZnFe_2O_4 + Fe^{2+} \tag{1}$$
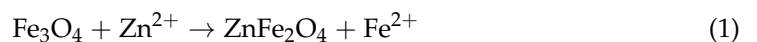
The different oxide structures and composition were observed when water chemistry (whether hydrogen or oxygen in solution) and materials were in difference. Fe_3O_4-$FeCr_2O_4$ double-layer oxide films were formed on the surface of 304 stainless steel when exposed to simulated primary water with hydrogen [11,14]. Because Ni percentage of 316L SS is a little higher than that in 304L SS (Table 1), the generation of $Ni_xFe_{1-x}O_4$ in outer layer and $Ni_{1-x}Fe_xCr_2O_4$ in inner oxide were also taken into consideration on the surface of stainless steel [15]. All in all, the particles of oxide film in outer layer were large, loose and uneven in size, while the inner oxides were small size and uniform [16,17]. Under Zn injection condition, $ZnFe_2O_4$ and $ZnCr_2O_4$ were generated as the main composition of oxide film on stainless steels. However, it has been reported by Liu et al. that, after a long-term oxidation, $ZnCr_2O_4$ became the dominant corrosion oxide. The possible main reaction equations were (1) as above and (2) (3) (4) as follows. It was generally acknowledged that the formation of the dense $Zn_xFe_{1-x}Cr_2O_4$ inner layer was the main reason for the improvement of corrosion resistance under a high temperature and high pressure water environment. Moreover, the replacement of Fe^{2+} by Zn^{2+} should be a no mixing limitation, but the ration of substitution depends on the concentration of Zn^{2+} and immersion time in the Zn-containing solution [11].

$$NiFe_2O_4 + Zn^{2+} \rightarrow ZnFe_2O_4 + Ni^{2+} \tag{2}$$

$$FeCr_2O_4 + Zn^{2+} \rightarrow ZnCr_2O_4 + Fe^{2+} \tag{3}$$

$$NiCr_2O_4 + Zn^{2+} \rightarrow ZnCr_2O_4 + Ni^{2+} \tag{4}$$

After long-term exposure to PWR high temperature coolants, oxide films with double-layer stable structure has also been found to be formed on the surface of nickel-based alloys (such as Alloy 600, Alloy 690, and Incoloy 800). It was believed that the selective release process of nickel resulted in the formation of the chromium-rich inner oxide layers. Some of the released nickel cations will be precipitated to form (Fe, Ni)-rich outer oxide particles, while others will be transported to, and activated in, the reactor core to increase the radiation fields [18]. Nickel-based alloy has high percentage of Ni in the matrix, and as a result, both outer and inner oxide are composed of Ni-rich oxide. It has been verified that $Fe_xNi_{1-x}Fe_2O_4$ inverse spinel was the main composition of outer layer and $Fe_xNi_{1-x}Cr_2O_4$ for inner layer. Similarly, $ZnFe_2O_4$ and $ZnCr_2O_4$ were expected to generate on Ni-based alloys with zinc injection by reaction (2) and (4). As shown in previous research, outer oxide particles were not densely packed but rather were unevenly dispersed.

In general, after zinc injection into PWR primary coolant, Zn^{2+} first enters the outer layer oxide and finally, to the inner layer oxide film. After the inner layer is saturated, a dynamic equilibrium will be established between the outer layer oxide and zinc in the solution. Therefore, it is necessary to calculate the thermodynamic data of Fe_3O_4, $NiFe_2O_4$, $FeCr_2O_4$, $NiCr_2O_4$, $ZnFe_2O_4$, and $ZnCr_2O_4$ and investigate the generation of each oxidation product under PWR primary circuit conditions.

The Gibbs free energy $\Delta G_f^\circ(T)$ of different substances and ions, involved in the calculation process at different temperature T, can be calculated by Equation (5):

$$\Delta G_f^\circ(T) = \Delta G_f^\circ(298K) - (T - 298.15) \times S_{298}^\circ + \int_{298}^{T} C_P dT - T \int_{298}^{T} \frac{C_P}{T} dT \tag{5}$$

where $\Delta G_f^\circ(298K)$ represents the Gibbs free energy at 298K, S_{298}° is the entropy value at 298K, and C_P is the heat capacity value, which can be calculated by Equation (6):

$$C_P = A + BT + CT^{-2} \tag{6}$$

where A, B, C are the heat capacity constants of different substances. All the thermodynamic data of species used in formation equations, obtained with the aforementioned method, are listed in Table 2.

Table 2. Thermodynamic data of species used in formation equations [2,11].

Species	$\Delta G_f^\circ(298K)$ (kJ·mol^{-1})	S_{298}° (J·mol^{-1}·K^{-1})	A	B ($\times 10^{-3}$)	C ($\times 10^5$)
Fe_3O_4	−1015.45	146.4	91.5	201	-
$NiFe_2O_4$	−974.6	125.9	77.4	235	1.42
$FeCr_2O_4$	−1347.02	147	163.2	22.36	−31.95
$NiCr_2O_4$	−1269.14	129.7	167.2	17.87	−21.05
$ZnFe_2O_4$	−1063.5	151.67	161.5	28.93	−26.53
$ZnCr_2O_4$	−1434.0	116.3	167.4	14.23	−25.1
Zn^{2+}	−147.1	−156.5	−164	-	-
Fe^{2+}	−78.9	−182.1	−188	-	-
Ni^{2+}	−48.2	−170.7	269.6	-	-

The Gibbs free energy $\Delta G_f^\circ(T)$ of each species at high temperatures from 473K (200 °C) to 623K (350 °C), as simulated with PWR primary conditions, are calculated by Equation (5) and listed in Table 3.

Table 3. Calculated $\Delta G_f^\circ(T)$ at different temperatures (kJ/mol).

Species	$\Delta G_f^\circ(473K)$	$\Delta G_f^\circ(523K)$	$\Delta G_f^\circ(563K)$	$\Delta G_f^\circ(573K)$	$\Delta G_f^\circ(623K)$
Fe_3O_4	−1048.13	−1059.81	−1069.83	−1072.43	−1085.95
$NiFe_2O_4$	−1003.65	−1014.31	−1023.53	−1025.92	−1038.47
$FeCr_2O_4$	−1379.03	−1390.21	−1399.72	−1402.18	−1414.87
$NiCr_2O_4$	−1298.62	−1309.19	−1318.24	−1320.57	−1332.70
$ZnFe_2O_4$	−1096.55	−1108.08	−1117.89	−1120.42	−1133.50
$ZnCr_2O_4$	−1460.99	−1470.79	−1479.21	−1481.39	−1492.71
Zn^{2+}	−112.57	−100.54	−90.35	−87.72	−74.19
Fe^{2+}	−38.85	−24.92	−13.13	−10.09	5.56
Ni^{2+}	−30.10	−28.49	−28.13	−28.16	−29.01

As the temperature rises from 473K to 623K, $\Delta G_f^\circ(T)$ of spinel oxides gradually decreases. Moreover, it is worth mentioning that $\Delta G_f^\circ(T)$ of $ZnCr_2O_4$ is lower than other substances formed on the surface of alloys, which directly indicates the high stability of $ZnCr_2O_4$ in aqueous systems at high temperatures.

According to the basic thermodynamic theory, when the Gibbs free energy change $\Delta G^\theta(T)$ is less than 0 under certain conditions, the reaction can proceed spontaneously. With zinc injection technology applied to PWR primary circuit, the double-layer oxide film composed of $ZnFe_2O_4$ and $ZnCr_2O_4$ are expected to be generated on the surface of alloys. The $\Delta G^\theta(T)$ of possible formation reactions of oxidation products are calculated by Equation (7) and shown in Figure 4 as a function of temperature.

$$\Delta G^\theta(T) = \Sigma v_i \Delta G_f^\circ(\text{Product}) - \Sigma v_i \Delta G_f^\circ(\text{Reactant}) \tag{7}$$
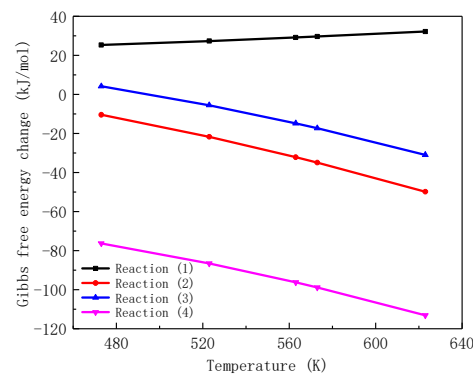
Figure 4. Gibbs free energy changes for $ZnFe_2O_4$ and $ZnCr_2O_4$ possible formation reactions.
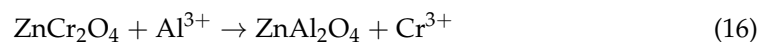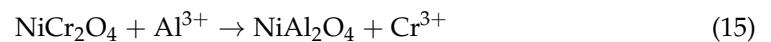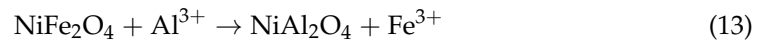
It can be seen in Figure 4 that, when temperature is higher than 500K, $\Delta G^\theta(T)$ of Reaction (2) (3) and (3) are negative, indicating the generation reaction can proceed spontaneously. As the temperature increases, the value of $\Delta G^\theta(T)$ decreases, which means the reactions are easier to occur in high temperature environments. Moreover, $\Delta G^\theta(T)$ of Reaction (4) behaves with the lowest value among these changes. From the thermodynamic point of view, the substitution reaction of $NiCr_2O_4$ (the replacement of Ni^{2+} by Zn^{2+}) is more likely to proceed under PWR primary circuit condition. The Gibbs free energy changes of Reaction (1) are positive, showing that this reaction cannot react spontaneously under the calculated condition. In consequence, the formation of $ZnFe_2O_4$ from Fe_3O_4 is analysed through the crystallographic properties of spinel.

2.2. Zinc-Aluminum Simultaneous Injection

Compared with zinc injection technology, Al^{3+} injection, alone, had a weaker corrosion inhibition effect. However, previous studies have shown that aluminium ion, injected into simulated PWR primary coolant, can effectively prevent the diffusion and deposition of Co^{2+}, enhance the corrosion activation energy of stainless steel, and solve the problem of

cumulative radiation [19]. Therefore, the experiments on the replacement of part of zinc by aluminium into PWR primary circuit water (that was called zinc-aluminium simultaneous injection (ZAWC)) were carried out. The results have proven that this new implement can further improve the corrosion resistance of metal materials on the basis of zinc injection in PWR primary circuit [20,21].

The formation of new phases, $ZnAl_2O_4$, $FeAl_2O_4$, and $NiAl_2O_4$, with high protectiveness in the passive film on the surface of carbon steel, stainless, and nickel-based alloys are the main reason for the enhancement of corrosion resistance. When zinc and aluminium are simultaneously injected, the following reactions may occur between the passive films and solution, in which (8)–(13) may be the reactions in outer layer and (14)–(16) for inner layer.

$$Fe_3O_4 + Zn^{2+} + 2Al^{3+} \rightarrow ZnAl_2O_4 + 2Fe^{3+} + Fe^{2+} \tag{8}$$

$$NiFe_2O_4 + Zn^{2+} + 2Al^{3+} \rightarrow ZnAl_2O_4 + 2Fe^{3+} + Ni^{2+} \tag{9}$$

$$Fe_2O_3 + ZnO + 2Al^{3+} \rightarrow ZnAl_2O_4 + 2Fe^{3+} \tag{10}$$

$$ZnFe_2O_4 + 2Al^{3+} \rightarrow ZnAl_2O_4 + 2Fe^{3+} \tag{11}$$

$$Fe_3O_4 + Al^{3+} \rightarrow FeAl_2O_4 + Fe^{3+} \tag{12}$$

$$NiFe_2O_4 + Al^{3+} \rightarrow NiAl_2O_4 + Fe^{3+} \tag{13}$$

$$FeCr_2O_4 + Al^{3+} \rightarrow FeAl_2O_4 + Cr^{3+} \tag{14}$$

$$NiCr_2O_4 + Al^{3+} \rightarrow NiAl_2O_4 + Cr^{3+} \tag{15}$$

$$ZnCr_2O_4 + Al^{3+} \rightarrow ZnAl_2O_4 + Cr^{3+} \tag{16}$$
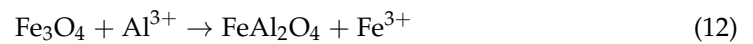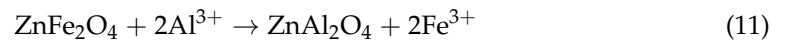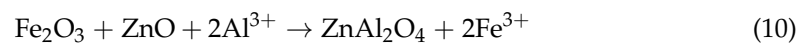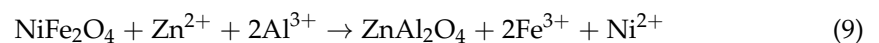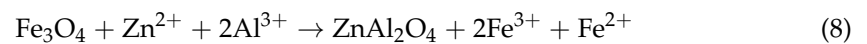
The calculation process is the same as Section 2.1. The thermodynamic data and $\Delta G_f^\circ(T)$ at different temperatures are listed in Tables 4 and 5.

Table 4. Calculated $\Delta G_f^\circ(T)$ at different temperatures (kJ/mol) [2,11,22–25].

Species	$\Delta G_f^\circ(298K)$ (kJ·mol^{-1})	S_{298}° (J·mol^{-1}·K^{-1})	A	B ($\times 10^{-3}$)	C ($\times 10^5$)
$ZnAl_2O_4$	−6671	87.03	166.52	15.48	−46.02
$FeAl_2O_4$	−1879.67	106.299	123.544	-	-
$NiAl_2O_4$	−1791.12	98.324	131.567	-	-
Fe^{3+}	−15.4	−382.5	−204	-	-
Al^{3+}	−485.3	−325	113.115	−0.506	-
Cr^{3+}	−215.48	−370.3	488.7	-	-
Fe_2O_3	−740.99	89.96	98.28	77.82	−14.85
ZnO	−321.9	43.16	47.58	3.93	−7.504

Table 5. Calculated $\Delta G_f^\circ(T)$ at different temperatures (kJ/mol).

Species	$\Delta G_f^\circ(473K)$	$\Delta G_f^\circ(523K)$	$\Delta G_f^\circ(563K)$	$\Delta G_f^\circ(573K)$	$\Delta G_f^\circ(623K)$
$ZnAl_2O_4$	−6692.04	−6699.99	−6706.89	−6708.69	−6718.10
$FeAl_2O_4$	−1903.65	−1912.13	−1919.35	−1921.21	−1930.82
$NiAl_2O_4$	−1814.05	−1822.34	−1829.43	−1831.27	−1840.76
Fe^{3+}	60.42	84.78	104.97	110.11	136.34
Al^{3+}	−433.34	−419.99	−409.70	−407.17	−394.85
Cr^{3+}	−171.95	−165.97	−162.88	−162.33	−160.83
Fe_2O_3	−761.66	−769.19	−775.67	−777.36	−786.13
ZnO	−331.31	−334.59	−337.38	−338.10	−341.81

The Gibbs free energy changes of Reaction (8)–(16) are calculated by Equation (7) at different temperatures, from 473K to 623K, and the data is shown in Figure 5.

Figure 5. Gibbs free energy changes of possible formation reactions: (**a**) Formation of $ZnAl_2O_4$, (**b**) Formation of $FeAl_2O_4$, $NiAl_2O_4$.
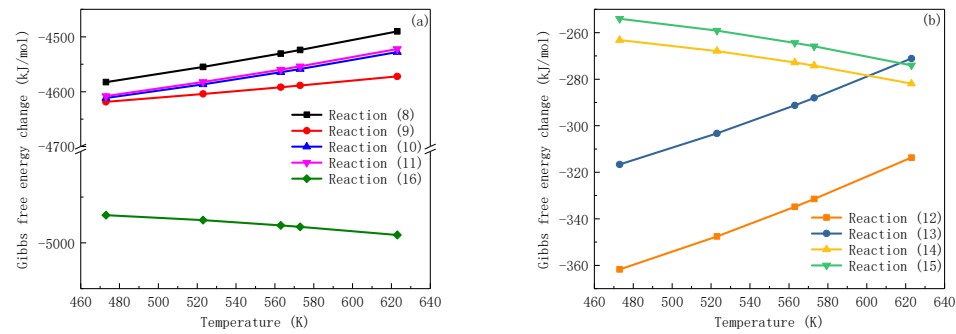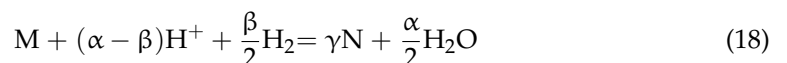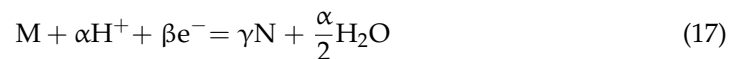
Firstly, the Gibbs free energy $\Delta G_f^\circ(T)$ of $ZnAl_2O_4$ is the lowest among oxides formed on alloys (Table 5), indicating the highest stability of this spinel oxide. Secondly, it can be seen that the Gibbs free energy changes in Figure 5a are significantly lower than (b), which means the high spontaneity of reaction of the formation of $ZnAl_2O_4$.

3. Solubility

The formation reactions of oxide films has been discussed above from the perspective of thermodynamics. In this chapter, the solubility of each substance in double-layer oxides are calculated to further investigate the stability of passive films formed on alloys, under ZWC and ZAWC conditions, at high temperatures. Moreover, the influences of zinc and zinc-aluminium injection on the corrosion resistance of different metals are also analysed.

3.1. Cr-Rich Inner Laryer Oxide

The solubility of $FeCr_2O_4$, $NiCr_2O_4$, and $ZnCr_2O_4$, formed in the inner layer oxide, are calculated using the method from K. Miyajima et al. [2]. Electrochemical process of spinel oxide M in aqueous systems can be expressed by Reaction (17), and the dissolution of solid M to produce ions in solution N can be written by general Reaction (18):

$$M + \alpha H^+ + \beta e^- = \gamma N + \frac{\alpha}{2}H_2O \tag{17}$$

$$M + (\alpha - \beta)H^+ + \frac{\beta}{2}H_2 = \gamma N + \frac{\alpha}{2}H_2O \tag{18}$$

The possible dissolution equilibrium reactions of $FeCr_2O_4$, $NiCr_2O_4$, and $ZnCr_2O_4$ are shown in Table 6 in the form of Reaction (18).

The thermodynamic data of each substance and ion are listed in Table 7, and the value of formation free energy changes $\Delta G^\theta(T)$ are calculated using Equation (7). The equilibrium constant can be used to calculate the activity of N (α_N). For low ionic strength solution, the activity coefficient is equal to 1, so α_N is equal to the concentration of ion N ([N]) and can be calculated by Equation (19):

$$\log_{10} \alpha_N = -\frac{\Delta G^\theta(T)}{2.303RT\gamma} - \frac{\alpha - \beta}{\gamma}pH_T + \frac{\beta}{2\gamma}\log_{10}P_{H_2} \tag{19}$$

where the value of hydrogen partial pressure $P_{H_2} = 0.1$ atm [19]. The total solubility of spinel oxide M is equal to the sum of ionic concentrations from the reactions, which contribute to the dissolution of M. Figure 6 shows the solubility of chromium-rich oxide formed in the inner layer at different temperature as a function of pH.

Table 6. Possible reactions of dissolution process.

Oxidation Product	Dissolution Equilibrium Reactions
$FeCr_2O_4$	(1)$FeCr_2O_4+2H^+ \rightarrow Fe^{2+}+Cr_2O_3+H_2O$ (2)$FeCr_2O_4+4H^++2H_2 \rightarrow Fe + 2Cr^{2+}+4H_2O$ (3)$FeCr_2O_4+H_2 \rightarrow Fe + 2CrO_2^-+2H^+$ (4)$FeO + 2CrO_2^-+2H^+ \rightarrow FeCr_2O_4+H_2O$ (5)$Fe_2O_3+4CrO_2^-+4H^++H_2 \rightarrow 2FeCr_2O_4+3H_2O$ (6)$Cr_2O_3+6H^+ \rightarrow 2Cr^{3+}+3H_2O$ (7)$Cr_2O_3+4H^++H_2 \rightarrow 2Cr^{2+}+3H_2O$ (8)$HFeO_2^-+H^+ \rightarrow FeO + H_2O$
$NiCr_2O_4$	(1)$NiCr_2O_4+2H^+ \rightarrow Cr_2O_3+Ni^{2+}+H_2O$ (2)$NiO + 2CrO_2^-+2H^+ \rightarrow NiCr_2O_4+H_2O$ (3)$NiO + 2CrO_4^{2-}+4H^++3H_2 \rightarrow NiCr_2O_4+5H_2O$ (4)$Cr_2O_3+6H^+ \rightarrow 2Cr^{3+}+3H_2O$ (5)$Cr_2O_3+4H^++H_2 \rightarrow 2Cr^{2+}+3H_2O$ (6)$HNiO_2^-+H^+ \rightarrow NiO + H_2O$ (7)$NiCr_2O_4+H_2 \rightarrow 2CrO_2^-+2H^++Ni$
$ZnCr_2O_4$	(1)$ZnCr_2O_4+8H^+ \rightarrow Zn^{2+}+2Cr^{3+}+4H_2O$ (2)$ZnCr_2O_4+6H^++H_2 \rightarrow Zn^{2+}+2Cr^{2+}+4H_2O$ (3)$ZnCr_2O_4+4H^++2H_2 \rightarrow Zn^{2+}+2Cr^{2+}+4H_2O$ (4)$ZnCr_2O_4+H_2 \rightarrow Zn + 2CrO_2^-+2H^+$ (5)$HZnO_2^-+2CrO_2^-+3H^+ \rightarrow ZnCr_2O_4+2H_2O$ (6)$HZnO_2^-+2CrO_4^{2-}+5H^++3H_2 \rightarrow ZnCr_2O_4+6H_2O$ (7)$ZnOH^++2CrO_4^{2-}+3H^++3H_2 \rightarrow ZnCr_2O_4+5H_2O$

Table 7. Thermodynamic data of species used in dissolution equations [2,11].

Species	$\Delta G_f^\circ (298K)$ (kJ·mol^{-1})	S_{298}° (J·mol^{-1}·K^{-1})	A	B ($\times 10^{-3}$)	C ($\times 10^5$)
H^+	0	−22.2	−71	-	-
H_2	0	130.6	27.28	3.264	0.502
H_2O	−237.19	70.08	75.44	-	-
Fe	0	27.15	14.1	29.7	1.799
FeO	−246.35	79.5	48.79	8.37	−2.803
$HFeO_2^-$	−379.18	41.92	−508.1	-	-
Cr_2O_3	−1046.84	81.17	119.3	9.096	−15.64
Cr^{2+}	−176.15	−120.9	314.5	-	-
CrO_2^-	−535.93	117.3	−386.7	-	-
CrO_4^{2-}	−736.8	80.33	−474	-	-
Ni	0	30.12	16.99	29.46	-
NiO	−215.94	37.99	−20.88	157.2	16.28
$HNiO_2^-$	−349.22	62.84	−409.7	-	-
Zn	0	41.63	22.38	10.04	-
$HZnO_2^-$	−464	62.84	−409.6	-	-
$ZnOH^+$	−329.28	−50.21	265.2	-	-

It can be generally seen, in Figure 6, that with the increase in pH, the solubility of Cr-rich oxides show a trend of first decreasing and then increasing. For $FeCr_2O_4$ and $ZnCr_2O_4$, with the increase in temperature from 473K to 623K, their solubility increases, indicating that the dissolution of these oxides are endothermic reaction. The lowest value displays at about pH = 6 at 473 K. As the temperature increases, the turning point shifts to the right side. However, the turning point of $NiCr_2O_4$ solubility occurs in the alkaline environment. When the pH is in the range of 7–8, the value of solubility behaves at a relatively low level.
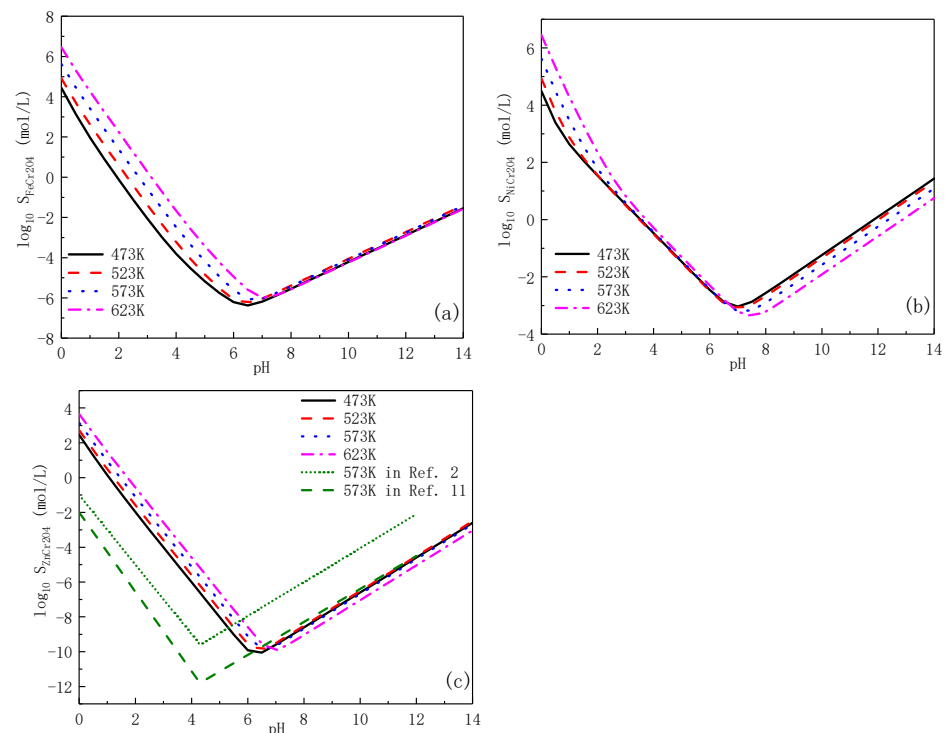
Figure 6. Solubility of $FeCr_2O_4$ (**a**), $NiCr_2O_4$ (**b**), and $ZnCr_2O_4$ (**c**) at different temperature as a function of pH.

The hydrogen partial pressure (P_{H_2}) in Equation (19) is necessary to calculate the solubility of oxides, so the difference between various studies were compared in Figure 6c. The hydrogen partial pressure of 0.252 atm was used in the calculation of K. Miyajima's research [2]. Due to the higher P_{H_2} value than this article, the solubility of $ZnCr_2O_4$ was relatively high, shown with short dots. However, the assumed P_{H_2} was in the range of 0.0019–0.1134 atm at 573.15K in Ref. [11], which was similar to the calculation above. Although the inflection point varies between references and this study, which may be due to the different ions and dissolution equilibrium reactions considered in the calculation, the overall trend of solubility was similar. When pH is higher than 6, especially in the pH range of PWR primary circuit coolant at 6.9–7.3, the value of solubility, it is very close to the calculated value (shown with dash line). It can be justified that the calculation results shown above were relatively credible.

3.2. Fe-Rich Outer Layer Oxide

The calculation method used for the solubility outer layer oxide Fe_3O_4, $NiFe_2O_4$, and $ZnFe_2O_4$ is from Shi et al. [20,26]. Firstly, it is assumed that $Fe_3O_4/NiFe_2O_4$ and Fe_2O_3 coexist in aqueous solution. After zinc injection is implanted, the dissolution reactions are based on the assumption of coexistence of $ZnFe_2O_4$ and $Fe(OH)_3$. The possible dissolution reactions are listed in Table 8, and the reaction equilibrium constant K can be calculated by Equation (20) according to the thermodynamic data shown in Table 9.

$$K = e^{-\frac{\Delta G^{\circ}(T)}{RT}} \qquad (20)$$

Table 8. Possible reactions of dissolution process.

Oxidation Product	Dissolution Equilibrium Reacuions
Fe_3O_4	$(1) Fe_3O_4 + 2H^+ \rightarrow Fe_2O_3 + Fe^{2+} + H_2O$ $(2) Fe_3O_4 + H^+ \rightarrow Fe_2O_3 + Fe(OH)^+$ $(3) Fe_3O_4 + H_2O \rightarrow Fe_2O_3 + Fe(OH)_2^0$ $(4) Fe_3O_4 + 2H_2O \rightarrow Fe_2O_3 + Fe(OH)_3^- + H^+$
$NiFe_2O_4$	$(1) NiFe_2O_4 + 2H^+ \rightarrow 2Fe_2O_3 + Ni^{2+} + H_2O$ $(2) NiFe_2O_4 + H^+ \rightarrow 2Fe_2O_3 + Ni(OH)^+$ $(3) NiFe_2O_4 + H_2O \rightarrow Fe_2O_3 + Ni(OH)_2^0$ $(4) NiFe_2O_4 + 2H_2O \rightarrow Fe_2O_3 + Ni(OH)_3^- + H^+$ $(5) NiFe_2O_4 + 3H_2O \rightarrow Fe_2O_3 + Ni(OH)_4^{2-} + 2H^+$
$ZnFe_2O_4$	$(1) ZnFe_2O_4 + 2H^+ + H_2O \rightarrow 2Fe(OH)_3 + Zn^{2+}$ $(2) ZnFe_2O_4 + H^+ + 3H_2O \rightarrow 2Fe(OH)_3 + Zn(OH)^+$ $(3) ZnFe_2O_4 + 4H_2O \rightarrow 2Fe(OH)_3 + Zn(OH)_2^0$ $(4) ZnFe_2O_4 + 5H_2O \rightarrow 2Fe(OH)_3 + Zn(OH)_3^- + H^+$ $(5) ZnFe_2O_4 + 6H_2O \rightarrow 2Fe(OH)_3 + Zn(OH)_4^{2-} + 2H^+$

Table 9. Thermodynamic data of species used in dissolution equations [27,28].

Species	$\Delta G_f^\circ (298K)$ $(kJ \cdot mol^{-1})$	S_{298}° $(J \cdot mol^{-1} \cdot K^{-1})$	A	B $(\times 10^{-3})$	C $(\times 10^5)$
$Fe(OH)^+$	-270.8	-120	450	-	-
$Fe(OH)_2$	-447.43	-80	435	-	-
$Fe(OH)_3^-$	-612.65	-70	560	-	-
$Ni(OH)^+$	-227.2	-49.7	-200	-	-
$Ni(OH)_2$	-406	-71	100	-	-
$Ni(OH)_3^-$	-586.5	-133	300	-	-
$Ni(OH)_4^{2-}$	-743.7	-252	460	-	-
$Fe(OH)_3$	-705.29	106.7	127.61	41.639	-42.17
$Zn(OH)^+$	-339.7	62.76	41.84	-	-
$Zn(OH)_2^0$	-519.27	61.55	33.47	-	-
$Zn(OH)_3^-$	-700.44	2.98	159.83	-	-
$Zn(OH)_4^{2-}$	-864.69	-27.51	89.54	-	-

The solubility of Fe-rich outer layer oxide is the sum of concentration of every ion and substance. Thus, the calculation equation can be expressed by Equations (21)–(28). In Equations (14)–(28), M represents the element of Fe, Ni, and Zn. Figure 7 demonstrates the solubility of Fe_3O_4, $NiFe_2O_4$, and $ZnFe_2O_4$, formed in the outer layer at different temperature, as a function of pH.

$$S_{Fe_3O_4} = \left[Fe^{2+} \right] + \left[Fe(OH)^+ \right] + \left[Fe(OH)_2^0 \right] + \left[Fe(OH)_3^- \right] \tag{21}$$

$$S_{NiFe_2O_4} = \left[Ni^{2+} \right] + \left[Ni(OH)^+ \right] + \left[Ni(OH)_2^0 \right] + \left[Ni(OH)_3^- \right] + \left[Ni(OH)_4^{2-} \right] \tag{22}$$

$$S_{ZnFe_2O_4} = \left[Zn^{2+} \right] + \left[Zn(OH)^+ \right] + \left[Zn(OH)_2^0 \right] + \left[Zn(OH)_3^- \right] + \left[Zn(OH)_4^{2-} \right] \tag{23}$$

$$\left[M^{2+} \right] = e^{-\frac{\Delta G_1^\circ}{RT} - (2\ln 10)pH} \tag{24}$$

$$\left[M(OH)^+ \right] = e^{-\frac{\Delta G_2^\circ}{RT} - (\ln 10)pH} \tag{25}$$

$$\left[M(OH)_2^0 \right] = e^{-\frac{\Delta G_3^\circ}{RT}} \tag{26}$$

$$\left[M(OH)_3^- \right] = e^{-\frac{\Delta G_4^\circ}{RT} + (\ln 10)pH} \tag{27}$$

$$\left[M(OH)_4^{2-} \right] = e^{-\frac{\Delta G_5^\circ}{RT} + (2\ln 10)pH} \tag{28}$$
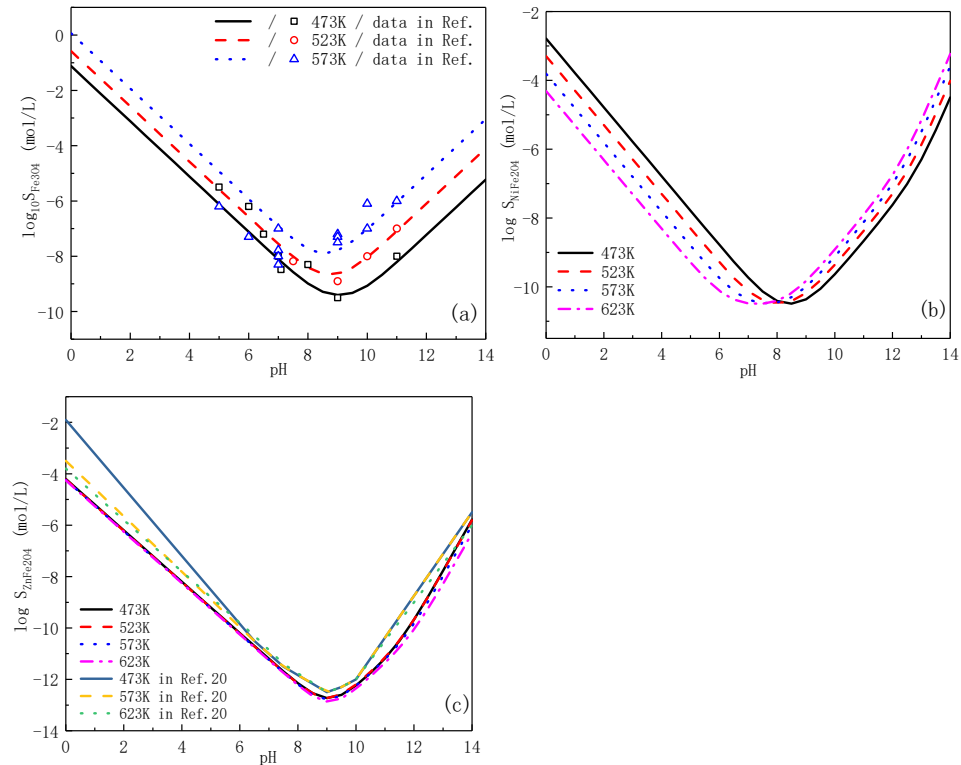

Figure 7. Solubility of Fe_3O_4 (**a**), $NiFe_2O_4$ (**b**), and $ZnFe_2O_4$ (**c**) at different temperature as a function of pH [20,27,29,30].

The solubility of Fe-rich oxides shows the same trend as Cr-rich oxides in Section 3.1 in that it decreases first and increases after pH is higher than 9. S_{Fe3O4} increases greatly under the elevation of temperature, while $S_{NiFe2O4}$ and $S_{ZnFe2O4}$ don't change obviously.

The comparison between this calculation method and the method similar to Cr-rich oxides were shown in Figure 7a. The solubility of magnetite was measured by experiments in dilute aqueous solutions saturated with H_2, and the results with 779 mol/kg H_2 at 473K, 523K, and 573K were labelled with hollow squares, circles, and triangles [27,29,30]. Although the calculation results in this study lack corresponding experiments to prove the accuracy, and the assumed equilibrium was slightly different, the ferrous ions were similar. Therefore, according to the comparison, the experimental data points in the references were near the calculated curves at high temperature, and it can be judged that the calculated method is feasible.

In addition, the solubility was close to Ref. [20] (shown in Figure 7c) in the pH range of PWR primary circuit environment, and the minimum solubility of $ZnFe_2O_4$ is close to 10^{-13} mol/L, which confirms the high stability of this spinel oxide at high temperatures. In consequence, according to the lower solubility of $ZnCr_2O_4$ and $ZnFe_2O_4$ than other oxides, it has verified that zinc injection technology enhances the corrosion resistance and stability of alloys used in PWR primary circuit

3.3. Al-Rich Oxide

The calculation of solubility of $ZnAl_2O_4$, $FeAl_2O_4$, and $NiAl_2O_4$ is similar to Section 3.2. It is assumed that Al_2O_3 and MAl_2O_4 (M represents Zn, Fe, and Ni) coexist in the solution [26]. The possible dissolution equilibrium reactions are presumed in Table 10.

The sum of ions solubility in aqueous solution composed the solubility of spinel oxides (Equations (29)–(31)), and the data is plotted in Figure 8 with the increase in temperature and pH.

Table 10. Possible reactions of dissolution process.

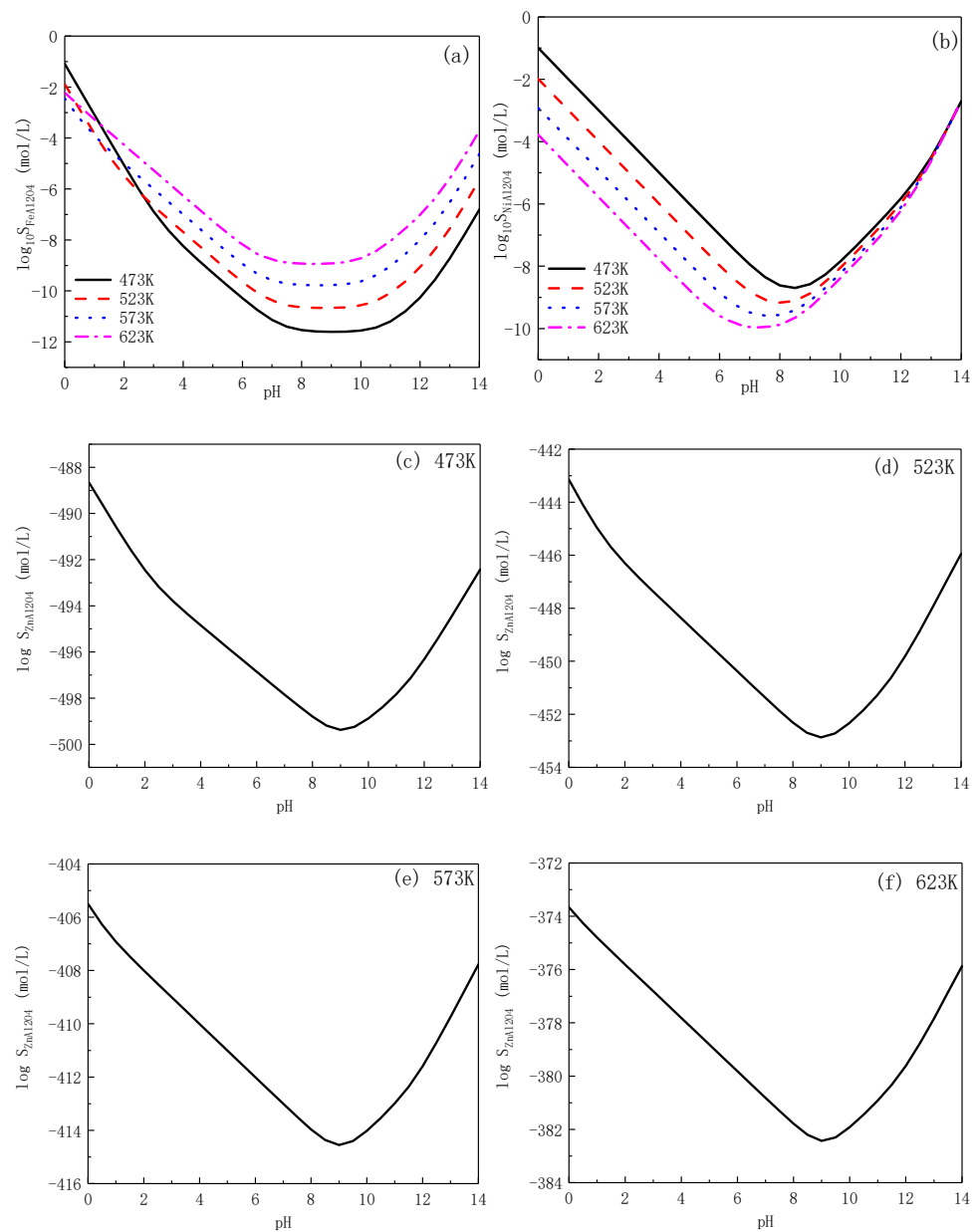| Oxidation Product	Dissolution Equilibrium Reactions
MAl_2O_4 (M: Zn, Fe, Ni)	$(1) MAl_2O_4 + 2H^+ \rightarrow Al_2O_3 + M^{2+} + H_2O$ $(2) MAl_2O_4 + H^+ \rightarrow Al_2O_3 + M(OH)^+$ $(3) MAl_2O_4 + H_2O \rightarrow Al_2O_3 + M(OH)_2^0$ $(4) MAl_2O_4 + 2H_2O \rightarrow Al_2O_3 + M(OH)_3^- + H^+$ $(5) MAl_2O_4 + 3H_2O \rightarrow Al_2O_3 + M(OH)_4^{2-} + 2H^+$

Figure 8. Solubility of $FeAl_2O_4$ (**a**), $NiAl_2O_4$ (**b**), and $ZnAl_2O_4$ (**c**–**f**) at different temperature as a function of pH.

$$S_{FeAl_2O_4} = \left[Fe^{2+}\right] + \left[Fe(OH)^+\right] + \left[Fe(OH)_2^0\right] + \left[Fe(OH)_3^-\right] + \left[Fe(OH)_4^{2-}\right] \tag{29}$$

$$S_{NiAl_2O_4} = \left[Ni^{2+}\right] + \left[Ni(OH)^+\right] + \left[Ni(OH)_2^0\right] + \left[Ni(OH)_3^-\right] + \left[Ni(OH)_4^{2-}\right] \tag{30}$$

$$S_{ZnAl_2O_4} = \left[Zn^{2+}\right] + \left[Zn(OH)^+\right] + \left[Zn(OH)_2^0\right] + \left[Zn(OH)_3^-\right] + \left[Zn(OH)_4^{2-}\right] \tag{31}$$

Given that the value of $S_{ZnAl2O4}$ is extremely small at high temperatures, the logarithm of $S_{ZnAl2O4}$ is calculated in Figure 8c–f. The lowest solubility of $ZnAl_2O_4$ among all spinel oxides demonstrates the highest stability in PWR primary circuit at high temperature. After zinc-aluminium is simultaneously injected into PWR coolant, the replacements of Fe^{2+}, Ni^{2+}, Cr^{3+} by Zn^{2+} and Al^{3+} react between the surface of alloys and the solution. $ZnAl_2O_4$, as the main product, with extremely low solubility and Gibbs free energy changes of Reaction (16) proves the positive effects of this new method on the improvement of corrosion resistance of structural materials. The effects of ZAWC on different materials are in difference, and the mechanism of the oxide film generation process is studied in the next chapter.

4. Mechanism Discussion

4.1. Thermodynamic Property

Figure 9 compares the solubility of various substances in the oxide film, formed on different alloys at a typical temperature of PWR primary circuit (573 K), and a typical water chemistry pH range ($pH_{300°C} = 6.9$~7.3).
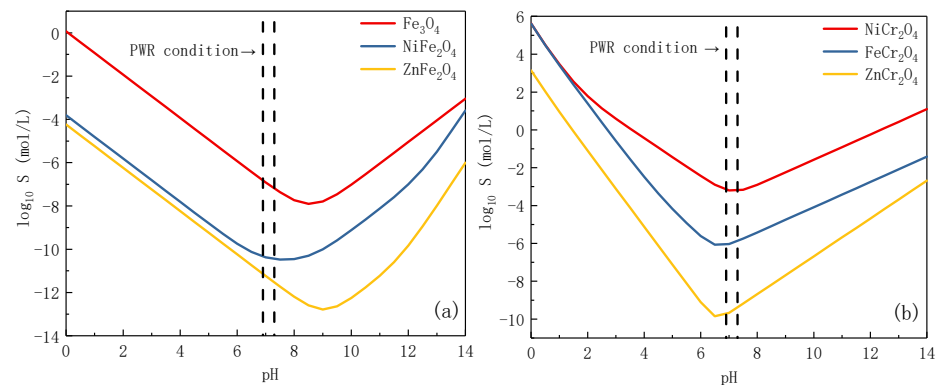

Figure 9. Comparison of solubility of oxides at PWR primary circuit condition: (**a**) Outer layer, (**b**) Inner layer.

Carbon steel is normally oxidized to form various iron oxides under PWR primary circuit water chemistry. When zinc is injected, the oxide (Fe_3O_4) reacts to form $ZnFe_2O_4$, which forms the spinel oxide on the surface of carbon steel. The solubility reduces dramatically from 10^{-7} mol/L (Fe_3O_4) to 10^{-11} mol/L ($ZnFe_2O_4$), which improves the corrosion resistance, and the spinel oxide film becomes more stable. When ZAWC is applied, $ZnAl_2O_4$ forms on the surface of carbon steel, and the solubility reduces sharply to 10^{-413} mol/L. Approximately 95% of the Fe in carbon steel (shown in Table 1) is considered to have the tendency to generate zinc ferrite and zinc aluminate, which directly enhance the corrosion resistance and stability.

Compared with carbon steel, the content of Cr and Ni in stainless steel increases to about 18% and 12%, respectively. However, Fe is still the main element. A double-layer Fe_3O_4-$FeCr_2O_4$ film forms on the surface under normal water chemistry. The outer layer is porous, composed of high iron and low nickel, and shows the properties of n-type semiconductor. The inner layer oxide is rich in chromium, relatively dense, and less porous, thus presenting p-type semiconductor properties. The corrosion mechanism of stainless

steel in high temperature water, proposed by J. Robertson, demonstrated that a duplex layered oxide was formed with the inner layer, growing by the centre of water along oxide micropores, and the outer layer, growing by the diffusion of metal ions. The corrosion rate was controlled by the solid state diffusion of Fe ions along grain boundaries in the oxide layer. The relatively fast diffusion of Fe and Ni through the oxide to the outer layer leads to the preferential dissolution of the steel. The outer layer forms at the oxide surface and is precipitated to relieve the supersaturation from the surrounding dissolution of metal ions [31].

The high temperature water environment with zinc injection promotes the formation of a thin and stable $ZnFe_2O_4$-$ZnCr_2O_4$ double layer film on the surface of stainless steel. The earlier zinc is added, the thinner the oxide films and the higher relative content of $ZnCr_2O_4$ in the film. The solubility of inner oxide decreases from 10^{-6} mol/L ($FeCr_2O_4$) to $10^{-9.7}$ mol/L ($ZnCr_2O_4$). It has been pointed out that, in the initial stage of oxidation, the growth rate of oxides on the surface of materials was relatively high. After long-term soaking in coolant, the growth rate decreased, and the stability of oxide films increased. The formation of a dense $Zn_xFe_{1-x}Cr_2O_4$ inner layer is the main reason for the corrosion resistance of component materials under ZWC condition. The replacement of Fe^{2+} and Ni^{2+} by Zn^{2+} can react with the inner and outer layers of oxides and, at the same time, Zn^{2+} enter the oxide films.

When zinc and aluminium are simultaneously injected into PWR coolant, it is shown in Figure 5 that the Gibbs free energy changes of Reaction (16) in the inner layer is the lowest among the formation reactions of $ZnAl_2O_4$ and decreases with the increase in temperature, that is to say that the generation of $ZnAl_2O_4$ in inner oxide may react more spontaneously in PWR primary circuit conditions. The extremely low value of $S_{ZnAl2O4}$ also improves the corrosion resistance of oxide films formed on stainless steel.

Nickel is the main element of Ni-based alloys, and $ZnFe_2O_4$-$ZnCr_2O_4$ double-layer oxide film is generated from $NiFe_2O_4$-$NiCr_2O_4$ under ZWC. The solubility decreases from 10^{-10} mol/L ($NiFe_2O_4$) to 10^{-11} mol/L ($ZnFe_2O_4$) for outer layer and 10^{-3} mol/L ($NiCr_2O_4$) to $10^{-9.7}$ mol/L ($ZnCr_2O_4$) in inner layer. This change in solubility is greater than $FeCr_2O_4$/$ZnCr_2O_4$, and the nickel content in Ni-based alloy is the highest among these materials. As a result, the zinc injection technology has more effective efforts on Ni-based alloys than carbon steel.

The free energy of formation of zinc-containing spinel is lower than that of corresponding zinc-free spinel. This means that the formation of $ZnCr_2O_4$, $ZnFe_2O_4$, and $ZnAl_2O_4$ are thermodynamically favoured over that of $FeCr_2O_4$, $NiCr_2O_4$, Fe_3O_4, $NiFe_2O_4$, $FeAl_2O_4$, and $NiAl_2O_4$ when the spinel are newly formed on the fresh metal surfaces. Based on thermodynamic calculations, $ZnCr_2O_4$ has not only a wider stable area in the potential-pH diagram but also a lower solubility under simulated PWR primary water conditions than other spinel [9,18].

4.2. Crystallographic Property

All the oxides formed on carbon steel, stainless steel, and Ni-based alloys discussed above are spinel oxides. The spinel structure of AB_2O_4 crystals was first determined in 1915 by Bragg [32] and Nishikawa [33]. The structure is face-centre cubic arrangement of oxygen ions, with metal ions occupying half of the octahedral and one-eighth of the tetrahedral interstitial sites within the anion sub lattice. It has been defined by Barth [34] that, if all the tetrahedral sites are occupied by A divalent cation ions and all the octahedral site by B trivalent ions, $A[B_2]O_4$, the structure is normal (N). On the other hand, if the tetrahedral sites are fully occupied by B ions and the octahedral sites are occupied by equal numbers of A and B ion, $B[AB]O_4$, which is called inverse (I). There is also a statistical distribution called random, in which the tetrahedral sites contain 1/3 A and 2/3 B cations, and the general formula can be written as $A_{1-v}^{n+}B_v^{m+}[A_v^{n+}B_{2-v}^{m+}]O_4^{2-}$.

The factors affecting the distribution of cations in spinel crystals are extremely complex, i.e., ion radius, ion charge, the configuration of electro layer, and so on. The radius of

metal cation ions are compared in Table 11 and the order of radius is $Al^{3+} < Ni^{2+} < Fe^{3+} < Cr^{3+} < Zn^{2+} < Fe^{2+}$. The lattice energy corresponding to different cations is listed in Table 12. The location of each element in the oxide is controlled by its corresponding diffusion rate in the spinel-type oxide. For stainless steel and Ni-based alloy, with zinc injection technology applied to PWR primary circuit, Cr-rich oxides are formed in the inner layer, and Cr^{3+} has the strongest octahedral lattice energy, which tends to occupy the octahedral sites. This results in Cr remaining in the inner layer due to its strong preference to occupy octahedral sites in spinel. At the same time, Zn^{2+} has the strongest tetrahedral lattice energy. Thus, diffusion rates through the oxide are slow, and $ZnCr_2O_4$ can be stable in the oxide film [35–37].

Table 11. Radius of metal cation ions (Å).

M^{2+}	Mg	Ni	Co	Zn	Fe	Mn
Radius	0.65	0.72	0.74	0.74	0.76	0.80
M^{3+}	Al	Ni	Co	Fe	Mn	Cr
Radius	0.50	0.62	0.63	0.64	0.66	0.69

Table 12. Lattice energy of metal cation ions.

Cation Ion	Lattice Energy of Octahedral Sites (kcal/mol)	Preferred Lattice
Cr^{3+}	16.6	Octahedral (strongest)
Ni^{2+}	9.0	Tetrahedral
Fe^{2+}	−9.9	Tetrahedral
Fe^{3+}	−13.3	Tetrahedral
Zn^{2+}	−31.6	Tetrahedral (strongest)

The types of different spinel oxides, formed on different metal materials under different simulated PWR water chemistry, are listed in Table 13. A positive SPE means the spinel is normal and the cation distribution is predicted to be more stable, while the negative value of SPE represents the inverse distribution is preferred. The value of TSE can judge the structural stability of spinel oxides. Therefore, the relatively lower TSE values of $ZnAl_2O_4$, $ZnCr_2O_4$, and $ZnFe_2O_4$ indicate the high stability of these three spinel, formed on alloys under ZWC and ZAWC conditions, which is consistent with the results analysed in Section 3.

Table 13. Crystallographic parameters of spinel oxides (eV).

Spinel	Type	Cation Distribution (tet, oct, oct)	Total Structure Energy (TSE)	Anion Preference Energy	Cation Preference Energy	Structure Preference Energy (SPE)
$FeAl_2O_4$	N	$Fe^{2+}Al^{3+}Al^{3+}$	−590.965	4.11	−0.82	2.06
$NiAl_2O_4$	I	$Al^{3+}Ni^{2+}Al^{3+}$	−619.534	4.23	−3.3	−1.43
$ZnAl_2O_4$	N	$Zn^{2+}Al^{3+}Al^{3+}$	−682.214	−0.04	2.45	1.76
$FeCr_2O_4$	N	$Fe^{2+}Cr^{3+}Cr^{3+}$	−638.243	1.67	−1.99	3.7
$NiCr_2O_4$	N	$Ni^{2+}Cr^{3+}Cr^{3+}$	−665.768	2.18	−4.5	0.61
$ZnCr_2O_4$	N	$Zn^{2+}Cr^{3+}Cr^{3+}$	−730.68	−2.04	1.29	3.84
Fe_3O_4	I	$Fe^{3+}Fe^{2+}Fe^{3+}$	−683.899	0	−0.14	−0.86
$NiFe_2O_4$	I	$Fe^{3+}Ni^{2+}Fe^{3+}$	−714.186	0.24	−2.67	−4.23
$ZnFe_2O_4$	N	$Zn^{2+}Fe^{3+}Fe^{3+}$	−775.186	−2.23	−3.14	0.77

In order to develop an understanding of why one cation arrangement is more stable than another physically, the components of the electronic contribution to the SPE can be examined, that is anion preference energy and cation preference energy. When A cation ion stabilizes the oxygen orbitals more than B cation, the oxygen preference energy will favour the normal structure, with A ions in tetrahedral sites. Otherwise, the oxygen preference energy favours the inverse spinel structure.

With Zn^{2+} and Al^{3+} in PWR coolant, the oxide formed on the surface of carbon steel are almost composed of $ZnAl_2O_4$, and in consequence, the effect of this new technology can significantly improve the stability of carbon steel. It has been reported before that the effect of ZAWC, on the improvement of corrosion resistance of Ni-based alloy, was not as obvious as that of carbon steel. Crystallographic properties may be an important basis for explaining this phenomenon. It is worth noting that the anion preference energy of $FeAl_2O_4$ and $NiAl_2O_4$ are significantly higher than $ZnAl_2O_4$, and as a result, Fe^{2+} and Ni^{2+} are easier to combine with the oxygen ions in the spinel, and the stability of bonding is higher. Due to the high content of Ni in Ni-based alloys and the Zn^{2+}/Al^{3+} concentration in solution that can enter the passive film to participate in the formation of spinel is limited, the presence of Ni^{2+} prevents Zn^{2+} from reactions, and $NiAl_2O_4$ is easier to generate than $ZnAl_2O_4$. Besides, $FeAl_2O_4$ can also produce in the oxide film, but due to the low percentage of Fe, the content of $FeAl_2O_4$ is less than $NiAl_2O_4$. The TSE of $NiAl_2O_4$ is lower than $ZnAl_2O_4$, and the solubility of $NiAl_2O_4$ is just a little lower than that of $NiFe_2O_4$-$NiCr_2O_4$, which formed in the normal PWR water chemistry, so the enhancement of corrosion resistance of Ni-based alloy is not obvious.

5. Conclusions

We investigated the inhabitation mechanism of ZWC and ZAWC on the corrosion of structural materials in PWR primary circuit. The $\Delta G^\theta(T)$ values of the reactions of Fe^{2+}, Ni^{2+} in oxide films replaced by Zn^{2+}, or Fe^{3+} replaced by Al^{3+} are extremely negative, and these replace reactions are highly spontaneous. Furthermore, we observe the solubility of $ZnAl_2O_4$ in high temperature water are extremely low, which contributes to the improvement in the corrosion resistance of carbon steels and stainless steels by the zinc-aluminium simultaneous injection into PWR primary coolant. On the other hand, the values of anion preference energy of $NiAl_2O_4$ and $FeAl_2O_4$ are much larger than that of $ZnAl_2O_4$ and Fe^{2+} and Ni^{2+} are easier to combine with the oxygen ions in the spinel than Zn^{2+} in $ZnAl_2O_4$. The concentration of Al^{3+} in the coolant is limited, so $NiAl_2O_4$ is formed, preferentially, on the surface of Ni-based alloy, and its content is greater than that of $ZnAl_2O_4$. Therefore, the corrosion resistance of Nickel alloys is mainly determined by the solubility and thermodynamic properties of $NiAl_2O_4$.

Author Contributions: Conceptualization, S.Z.; Methodology, Y.J. and S.Z.; Software, Y.J.; Validation, S.Z.; Investigation, Y.T.; Data curation, Y.J.; Writing—original draft preparation, Y.J.; Writing—review and editing, S.Z. and Y.T. All authors have read and agreed to the published version of the manuscript.

Data Availability Statement: The data presented in this study are openly available in [ResearchGate] at [10.5573/ieek.5013.50.1.034], reference number [2]; in [Elsevier] at [10.1016/j.corrsci.2011.06.011] [10.1016/S0016-7037(96)00339-0] [10.1016/S0010-938X(96)00067-4], reference number [11,25,27]; in [Springer] at [10.1023/A:1021866025627] [10.1007/BF00645517], reference number [28,29].

Conflicts of Interest: The authors declare no conflict of interest.

References

1. Calvar, M.L.; Curieres, I.D. Corrosion issues in pressurized water reactor (PWR) systems. *Nucl. Corros. Sci. Eng.* **2012**, 473–547. [CrossRef]
2. Miyajima, K.; Hirano, H. Thermodynamic consideration on the effect of zinc injection into PWR primary coolant for the reduction of radiation buildup and corrosion control. In Proceedings of the CORROSION 2001, Houston, TX, USA, 11–16 March 2001.
3. Scott, P.M.; Combrade, P. General corrosion and stress corrosion cracking of Alloy 600 in light water reactor primary. *J. Nucl. Mater.* **2019**, *524*, 340–375. [CrossRef]
4. Liu, X.; Hwang, W.; Park, J.; Van, D.; Chang, Y.; Lee, S.H.; Kim, S.-Y.; Han, S.; Lee, B. Toward the multiscale nature of stress corrosion cracking. *Nucl. Eng. Technol.* **2018**, *50*, 1–17. [CrossRef]
5. Terachi, T.; Fujii, K.; Arioka, K. Microstructural characterization of SCC crack tip and oxide film for SUS 316 stainless steel in simulated PWR primary water at 320 °C. *J. Nucl. Sci. Technol.* **2005**, *42*, 225–232. [CrossRef]

6. Ziemniak, S.E.; Hanson, M. Corrosion behavior of 304 stainless steel in high temperature hydrogenated water. *Corros. Sci.* **2002**, *44*, 2209–2230. [CrossRef]

7. Staehle, R.W. QMN approach to SCC mechanism prediction-starting third meeting. In Proceedings of the 15th International Conference on Environmental Degradation of Materials in Nuclear Power Systems—Water Reactors, Colorado Springs, CO, USA, 7–11 August 2011.

8. Xiahe, L.; Xinqiang, W.; Enhou, H. Status and progress on study of corrosion behavior of structural materials in Zn-injected water for LWRs. *Corros. Sci. Prot. Technol.* **2011**, *23*, 287–292.

9. Holdsworth, S.; Scenini, F.; Burke, M.G.; Bertali, G.; Ito, T.; Wada, Y.; Hosokawa, H.; Ota, N.; Nagase, M. The effect of high-temperature water chemistry and dissolved zinc on the cobalt incorporation on type 316 stainless steel oxide. *Corros. Sci.* **2018**, *140*, 241–251. [CrossRef]

10. Huang, J.; Liu, X.; Han, E.-H.; Wu, X. Influence of Zn on oxide films on Alloy 690 in borated and lithiated high temperature water. *Corros. Sci.* **2011**, *53*, 3254–3261. [CrossRef]

11. Xiahe, L.; Xinqiang, W.; Enhou, H. Influence of Zn injection on characteristics of oxide film on 304 stainless steel in borated and lithiated high temperature water. *Corros. Sci.* **2011**, *53*, 3337–3345.

12. Zhang, S.; Shi, R.; Chen, Y.; Wang, M. Corrosion behavior of oxide films on AISI 316L SS formed in high temperature water with simultaneous injection of zinc and aluminum. *J. Alloys Compd.* **2018**, *731*, 1230–1237. [CrossRef]

13. Chenhao, S. Effect of Zinc and Aluminum Simultaneous Injection on Corrosion Behavior of Structure Materials in PWR. Ph.D. Thesis, North China Electric Power University, Beijing, China, 2021.

14. Kim, Y.-J. Analysis of Oxide Film Formed on Type 304 Stainless Steel in 288 °C Water Containing Oxygen, Hydrogen, and Hydrogen Peroxide. *Corrosion* **1999**, *55*, 81–88. [CrossRef]

15. Kim, Y.-J. Characterization of the Oxide Film Formed on Type 316 Stainless Steel in 288 °C Water in Cyclic Normal and Hydrogen Water Chemistries. *Corrosion* **2012**, *51*, 849–860. [CrossRef]

16. Na, L. Influence of Water Chemistry on Corrosion Behavior of 304 Stainless Steel in High Temperature High Pressure Solution. Master's Thesis, Tianjin University, Tianjin, China, 2012.

17. Cissé, S.; Laffont, L.; Tanguy, B.; Lafont, M.-C.; Andrieu, E. Effect of surface preparation on the corrosion of austenitic stainless steel 304 L in high temperature steam and simulated PWR primary water. *Corros. Sci.* **2012**, *56*, 209–216. [CrossRef]

18. Lim, D.-S.; Jeon, S.-H.; Bae, B.J.; Choi, J.; Song, K.M.; Hur, D.H. Effect of zinc addition scenarios on general corrosion of Alloy 690 in borated and lithiated water at 330 °C. *Corros. Sci.* **2021**, *189*, 10927. [CrossRef]

19. Xiaofang, S. Influence of Aluminum Ion on Corrosion Behavior of Stainless Steel in High Temperature Water of Nuclear Power Plant. Ph.D. Thesis, North China Electric Power University, Beijing, China, 2018.

20. Rongxue, S. Electrochemical Research on Mechanism of Corrosion Resistance of Oxide Films on Fe-Base Alloys. Ph.D. Thesis, North China Electric Power University, Beijing, China, 2018.

21. Shenghan, Z.; Chenhao, S.; Yu, T. Influence of zinc and aluminum simultaneous injection on corrosion behavior and semiconducting properties of oxide film on 304 L. *Int. J. Electrochem. Sci.* **2020**, *15*, 9874–9887.

22. Dean, J.A. *Lange's Handbook of Chemistry*, 15th ed.; McGraw-Hil: New York, NY, USA, 1998.

23. Barin, I. *Thermochemical Data of Pure Substances*; VCH: Weinheim, Germany, 1996; pp. 1–103.

24. Chen, C.M.; Aral, K.; Theus, G.J. *Computer-Calculated Potential PH Diagrams to 300 °C*; EPRI: Palo Alto, CA, USA, 1983.

25. Shock, E.L.; Sassani, D.C.; Willis, M.; Sverjensky, D.A. Inorganic species in geologic fluids: Correlations among standard molal thermodynamic properties of aqueous ions and hydroxide complexes. *Geochim. Cosmochim. Acta* **1997**, *61*, 907–950. [CrossRef]

26. Shenghan, Z.; Chenhao, S.; Yu, T. Corrosion behavior of high-strength low-alloy steel in high-temperature water with zinc and aluminum simultaneous injection. *Corrosion* **2020**, *76*, 919–929.

27. Beverskog, B.; Puigdomenech, I. Revised pourbaix diagrams for iron at 25–300 °C. *Corros. Sci.* **1996**, *38*, 2121–2135. [CrossRef]

28. Bénézeth, P.; Palmer, D.A.; Wesolowski, D.J.; Xiao, C. New measurements of the solubility of zinc oxide from 150 to 350 °C. *J. Solut. Chem.* **2002**, *31*, 947–973. [CrossRef]

29. Tremaine, P.R.; LeBlanc, J.C. The solubility of magnetite and the hydrolysis and oxidation of Fe^{2+} in water to 300 °C. *J. Solut. Chem.* **1980**, *9*, 415–442. [CrossRef]

30. Sweeton, F.H.; Baes, C.F., Jr. The solubility of magnetite and hydrolysis of ferrous ion in aqueous solutions at elevated temperatures. *J. Chem. Thermodyn.* **1970**, *2*, 479–500. [CrossRef]

31. Robertson, J. The Mechanism of High Temperature Aqueous Corrosion of Stainless Steels. *Corros. Sci.* **1991**, *32*, 443–465. [CrossRef]

32. Bragg, W.H. The Structure of Magnetite and the Spinels. *Nature* **1915**, *95*, 561. [CrossRef]

33. Nishikawa, S. Structure of Some Crystals of Spinel Group. *Proc. Tokyo Math.-Phys. Soc.* **1916**, *8*, 199–209.

34. Barth, T.F.W.; Posnjak, E. Spinel structures: With and without variate atom equipoints. *Z. Kristallogr.* **1932**, *82*, 325. [CrossRef]

35. Han, M.; Wang, Z.; Xu, Y.; Wu, R.; Jiao, S.; Chen, Y.; Feng, S. Physical properties of $MgAl_2O_4$, $CoAl_2O_4$, $NiAl_2O_4$, $CuAl_2O_4$, and $ZnAl_2O_4$ spinels synthesized by a solution combustion method. *Mater. Chem. Phys.* **2018**, *215*, 251–258. [CrossRef]

36. Guoliang, J. Studies on the Fabrication and Application of Oriented Mixed Metal Oxide Films Derived from Layered Doubled Hydroxides. Master's Thesis, Beijing University of Chemical Technology, Beijing, China, 2009.

37. Lei, J. *Research and Application of Zinc Injection in PWRs*; Progress Report on China Nuclear Science & Technology: Guiyang, China, 2011.